MECHANO-ELECTROCHEMISTRY OF NICKEL TITANIUM ALLOY

By

Deanna Schauben

Thesis

Submitted to the Faculty of the

Graduate School of Vanderbilt University

in partial fulfillment of the requirements

for the degree of

MASTER OF SCIENCE

in

Mechanical Engineering

May, 2017

Nashville, Tennessee

Approved:

Cary L. Pint, Ph.D.

Ravindra Duddu, Ph.D.

Douglas Adams, Ph.D.

ACKNOWLEDGEMENTS

First, I would like to thank Dr. Cary Pint for his continued support and guidance during the past three years. I thank Dr. Ravindra Duddu and Dr. Douglas Adams for agreeing to be a part of my thesis committee. I am extremely grateful to Nitin Muralidharan for his indispensable contributions and mentorship. I thank Adam Cohn, Keith Share, and Andrew Westover for important discussions in fine-tuning experimentation and interpretation of results. I thank Rachel Carter, Anna Douglas, Mengya Li, Landon Oakes, and Kathleen Moyer for useful conversations regarding the results of this work. I also thank Robin Midgett for significant contribution to cell design, custom machining services, and equipment troubleshooting. I thank Dr. Rizia Bardhan for the generous use of Raman Confocal microscope and lab facilities and Dr. Greg Walker for consultations regarding heat transfer. Additionally, I thank Ryan Froehling for assistance in the lab and Kelsay Neely for assistance with formatting. Finally, I thank my parents for their love and encouragement throughout my undergraduate and graduate career at Vanderbilt University.

Table of Contents

LIST OF FIGURES

Figure Page

CHAPTER I

INTRODUCTION

Nitinol (NiTi) is an alloy that was developed in 1959 in the Naval Ordinance Laboratory with applications in transducers, actuators, heat engines, and medical and dental devices. It is known and used for its superelastic and shape-memory properties, both of which made possible by its nearly equiatomic composition. Superelasticity refers to its ability to be deformed to approximately 8% recoverable strain, and upwards of 15% strain before mechanical failure. Shape memory refers to the property that, upon activation and deformation below 8% strain, NiTi will recover its original shape with application of heat. These properties stem from the arrangement of nearly-equiatomic component atoms that are arranged in a simple interpenetrating cubic structure in its parent phase (austenite) or in an asymmetric monoclinic phase (martensite). The latter structure initially contains twin planes after transforming from martensite, but upon continued application of stress it undergoes a reorientation process known as de-twinning; this transformation and reorientation are what allow the alloy to accommodate such high degrees of extension without damaging the structure or causing slip, making the deformation recoverable.

When activated for superelasticity and strained in a tensile mode, NiTi follows a characteristic deformation profile in four Stages. In Stage I, the parent phase austenite deforms elastically; Stage II is the stress-induced martensitic (SIM) transformation, in which grains of austenite exothermically reorient to twinned martensite via the propagation of a shear band front[1-8] and the two phases coexist; grains of martensite finish reorienting and de-twinning in Stage III; finally, the oriented martensite plastically deforms in Stage IV.[1,2] The first three Stages are illustrated in Figure 1. The transformation of austenite to martensite may progress by the

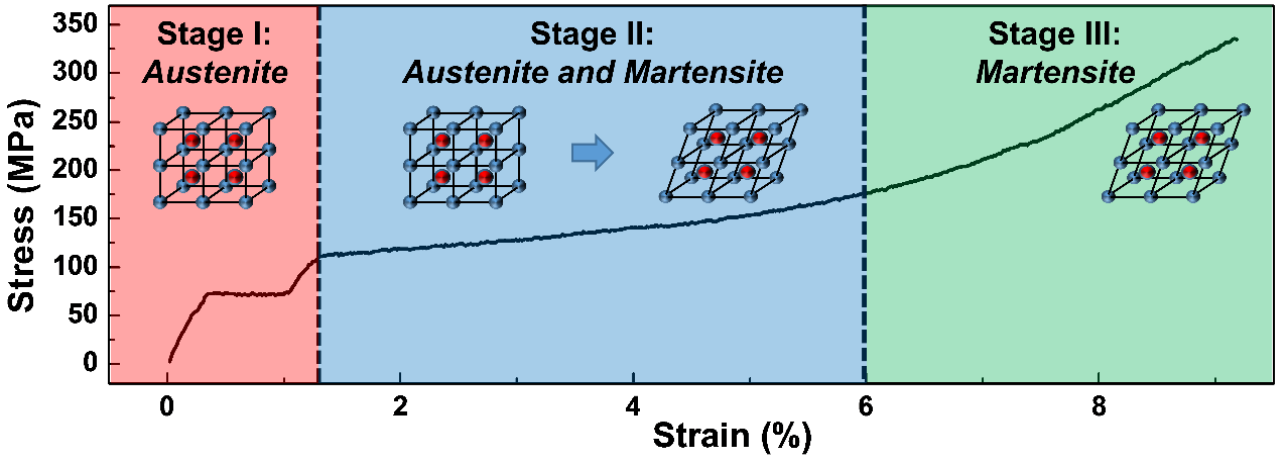

Figure 1: A representative stress-strain curve of NiTi with unit cells of the phase(s) present in each Stage depicted pictorially.

advancement of a shear band front with locally elevated internal stress[4] or in a discontinuous, highly localized mode in which favorably oriented grains transform preferentially[26].[1-8] Additionally, the shear band is the boundary between the portion of the specimen with strain corresponding to the end of the transformation and the portion with that corresponding to the beginning.[4] These Stages are not absolutely distinguished by the content of different phases. While martensite does not typically appear before Stage II, residual pockets of austenite can be found even in Stage III, after the SIM plateau region of the stress-strain curve has ended.[1,2] Additionally, oriented martensite production continues into Stage III,[1] as indicated by improved strain recovery for specimens strained to this Stage compared to Stage II[5,9].

Deformed NiTi exhibits a shape memory property when heated above a transformation temperature, but this is not the only way in which thermal effects influence the structure and behavior of NiTi. The rate of straining and the exothermic nature of the first-order phase transformation are related factors that may significantly increase the temperature of a NiTi sample undergoing strain.[2,3,10-13] As high-temperature austenite transforms to low-temperature martensite at a propagating interface or in local regions, it releases latent heat that in turn raises the

temperature of the sample (depending on the velocity of the interface compared to heat transfer within the sample), as well as the stress needed to continue the transformation.[3,10-13] At higher strain rates, thermal effects – such as changes in temperature, SIM critical stress, slope of the stress plateau, thermal softening, and superelasticity – are increased as the process becomes more adiabatic.[10-13] In fact, any change in stress-strain behavior of NiTi at higher strain rates can be attributed almost entirely to the involvement of thermal effects, and there are no strain rate-dependent effects for room temperature quasi-static (taken here to be synonymous with isothermal) processes.[10,11] The rate chosen to represent a quasi-static process in this investigation is in agreement with literature, particularly considering that it takes place mostly in a liquid.[2,3,10-13]

Strain engineering and mechano-electrochemistry are related emerging fields bridging mechanical manipulation and electrochemical properties. Many groups have found that strain can be imparted to a material of interest through the use of a (typically superelastic or shape-memory) substrate to alter the electronic structure and magnetism[14], catalytic properties[15,16], chemical potential difference[17], and reaction peak shifts[18]. Such investigations have proven the viability and importance of mechano-electrochemistry and have begun characterizing the effects of compressive and tensile strains, but most do not consider in-situ strain effects or experimental strains larger than 3.5% for tension or 7.5% for compression[16] due to the inability to impart more across the interface between the substrate and the sample. Furthermore, the effect of strain on the magnetization[19], potentiodynamic polarization[19,20], and EIS measurements[20] of steels is also receiving attention. Guo et al found that the corrosion potential and passivation current density both increased with strain[19], which indicates facilitated corrosion and oxide formation. Liu et al found that strain rate did not affect the corrosion potential, and elastic strain did not affect the bulk electrochemical properties of the steel.[20]

Rather than using it only as a substrate with which to impart strain to other materials, some groups have investigated the mechano-electrochemistry of NiTi and its native oxide in-situ during straining; many of these papers pertain to biomedical applications. The open circuit voltage (OCV), fatigue behavior, and involvement of a surface oxide have been of particular interest[4,21,22], as well as corrosion properties[23-25]. Typically, change in OCV is linked to cracking of the surface oxide and facilitated passivation of newly exposed metal beneath said oxide, particularly when analyzed through the lens of high cyclic loading and long-term behavior.[4,21,22] This focus on surface oxide behavior in prior research is due to these biomedical applications which necessitate a stable TiO_2 layer to prevent Nickel from leeching into the body. Rondelli et al and Heßin found that local corrosion resistance of NiTi is not significantly affected by the presence of stress-induced martensite[23,26] and Huang found that tensile load did not have an appreciable effect on corrosion parameters (however, the load did not exceed 2 N or 12 MPa, which corresponds to approximately 0.03% strain)[25]. Montero-Ocampo et al found that compressive strains improved corrosion resistance.[24] Racek et al found that crack formation and opening/closing during cyclic loading facilitates localized corrosion.[21]

In the context of electrochemistry, the open circuit voltage (OCV), a property of a specimen, is a rest potential (measured against a reference) at which there is no current in the system. It has been equated to the corrosion potential.[4,28] The OCV gives a measure of the potential difference between the surface of the specimen and the immediate electrolyte environment in which it is submerged when oxidation and reduction reactions are in quasi-equilibrium (higher OCV indicates progression of oxidation and passivation, while lower OCV indicates progression of reduction).[4] Therefore, this parameter lends insight into surface reactivity and the kinetics of passivation[22], as well as the affinity for electrochemical corrosion (higher OCV indicates

facilitated corrosion). On a Tafel curve used to characterize corrosion, the OCV corresponds to the corrosion potential, at which the anodic and cathodic reactions occur at the same rate (anodic and cathodic currents are equal and opposite, resulting in no net current). The OCV can be affected by the selection of metal and electrolyte, surface properties, temperature, and exposure time;[4] therefore, when these parameters remain constant, any change in OCV is attributable only to an alteration of the metal's material properties. For NiTi samples with a surface oxide, the OCV falls at the start of the SIM plateau due to the nucleation and propagation of the shear band front[4,22] and increases at approximately 3% strain due to the passivation of exposed metal at freshly opened cracks[4]. Potential and energy are related by the Nernst equation, $V = -\frac{\Delta G}{nF}$, in which V is the potential, ΔG is the Gibbs free energy, n is the number of electrons involved, and F is the Faraday constant. If the potential increases, the Gibbs free energy decreases, signifying that the reaction in question is more favorable and may occur more easily. The OCV is therefore a measure of how favorable a corrosion or passivation reaction is.

In this work, we scrutinize the changes in OCV throughout Stages I-III of the stress-strain profile of polished NiTi, with particular attention to the SIM plateau. To do so, it was necessary to first design and build an in-situ electrochemical cell that could be utilized in conjunction with a load frame without leaking electrolyte or interfering with the deformation of NiTi samples. The OCV behavior during straining was examined at two strain rates, and the steady state response was examined for multiple samples, each strained to a different point on the stress-strain profile. It was found that samples strained to within Stage I exhibited a permanent change of about 7 mV, those strained to within Stage II exhibited a permanent change of about -25 to -45 mV, and those strained to within Stage III exhibited a permanent change of about -2 to 6 mV. The maximum change in OCV (found just after the beginning of Stage II) fell between about -50 and -75 mV. In focusing

on the behavior of the metal alloy itself rather than using it as a substrate or monitoring a surface oxide, this work lends insight into facilitated corrosion or other (electro-)chemical processing and previously unexplored energetic concomitants of morphological phase transformation.

CHAPTER II

CELL AND EXPERIMENTAL DESIGN

Cell, Secondary Containment, and Grip Development

In order to perform in-situ electrochemistry analysis while the samples were strained, a specialized cell that could be used with the equipment on hand (Instron TTC-02ML load frame) was required. The requirements for such a cell were: chemically resistant to corrosive electrolyte (KOH); lightweight enough such that the weight of the cell does not introduce significant strain to the sample; watertight seal that allows free sliding and deformation of the sample; deep enough to securely accommodate the reference electrode (SCE); easy insertion of sample as not to introduce bending or compressive strain; and stability during straining. It was also necessary to devise a secondary containment measure in case of spills or failure.

The original design concept was a rectangular block with a central well through which the sample would be passed. The tension in the sample, introduced by gripping both exposed ends of it in the load frame, was the mechanism that would hold the cell upright and stable. The counter electrode (Platinum foil) would be clipped to the inside wall of the cell using an alligator clip, and the reference electrode (SCE) would rest loosely inside the well. The material chosen for the cell was Polytetrafluoroethylene (McMaster-Carr Teflon PTFE Rectangular Bar) due to its resistance to corrosion, and the secondary containment was made from a polypropylene bin (Sterilite 6 Quart Storage Box). Bulk Teflon was machined to design specifications in the in-house machine shop using a hydraulic horizontal band saw, a mill, and a drill press.

The first prototype of the cell (Figure 2) included one main central well milled to a depth and a through hole at the base of the well. A tapered rubber plug (McMaster-Carr Chemical-Resistant Rubber Plug) had a hole drilled in the center and was hammered into the hole of the

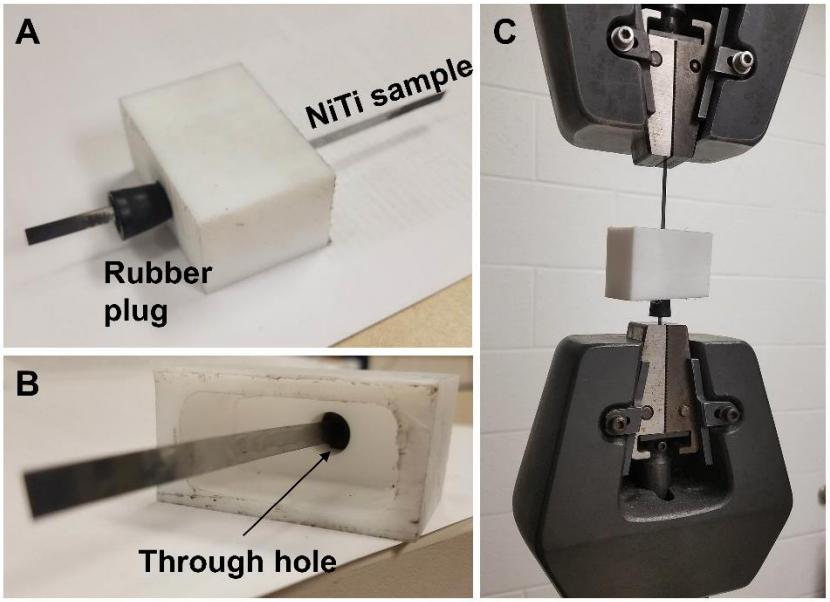

Figure 2 : Photographs of the first in-situ cell prototype. (A) Side view. (B) Top view. (C) The prototype mounted in the load frame grips with the sample pulled just taut.

cell. This was intended to allow movement of the sample and prevent leaks; however, the plug was very difficult to drill, caused unavoidable bending and other deformation of the sample upon insertion, and did not prevent leaks. Therefore, the second prototype replaced the drilled, tapered plug with a flat septum (VWR Plain Septa for Open Top Caps, Wheaton, PTFE faced silicone) with a narrow slit cut with a razor. It also introduced a shallow well at the base of the cell to house the septum. In this prototype, the septum was attached to the cell with fast-curing epoxy (PC-Clear Clear Liquid Epoxy) and allowed to cure for several hours. The reference electrode did not sit securely in this prototype due to the tension in the wire connecting it to the potentiostat (Metrohm Autolab PGStat101).

The third prototype added an off-central well within the main well to house the reference electrode and prevent it from sliding within the cell. Because the septa attached with epoxy pulled off with little force, the septum in this prototype was attached using vacuum tape (Fiberglass Supply Roll Y-24 Sealant Tape) from composite layups (see Figure 6B). This

strategy was selected because vacuum tape is airtight, reusable, moldable, and highly flexible, meaning it successfully prevents leaks around the edges of the septum and cannot peel off during straining. A comparison of the strain profile from a freely strained sample and samples strained within the first and third prototypes of the cell (Figure 3) shows that the final prototype of the cell does not significantly interfere with this process.

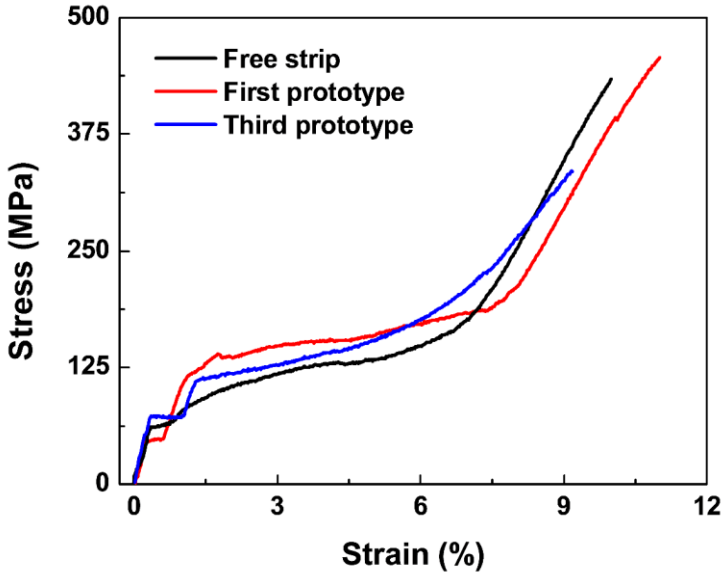

Figure 3 : Comparison of stress-strain curves of a polished sample strained freely and polished samples strained while mounted in the in-situ cell prototypes.

The final version of the cell setup (Figure 4) included two septa with a layer of vacuum putty between them (not pictured) to prevent leakage from the slit in the original septum. It was also machined to optimized wall thickness, reference electrode well depth, and base thickness. This design performed admirably, so long as the septa and vacuum tape were replaced after every 3-4 uses.

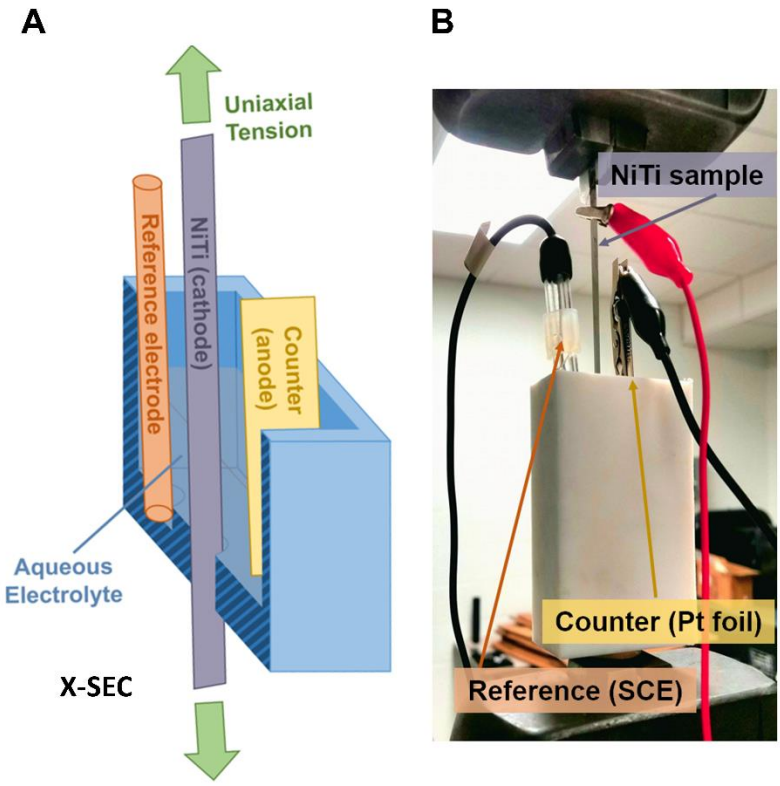

Figure 4: The final version of the in-situ cell and three electrode system. (A) A schematic diagram of the cross-section. (B) A photograph of the in-situ cell and three electrode system mounted in the load frame grips with the sample pulled just taut.

The secondary containment (Figure 5) took the form of a plastic bin (34.6 cm x 21 cm x 12.4 cm) with a large slit cut into the bottom with a box cutter. The bottom of the sample was fed through this slit, which was then sealed with more vacuum tape. The bottom of the cell was propped up with rectangular pieces of scrap 1018 steel, and nickel-plated neodymium magnet cubes were placed at the top surface of the lower load frame grip. The bin was then placed on the grip, with the sample fitting between the gripping surfaces and the steel directly above the magnets. This secured the bin to the lower grip tightly – with an added benefit of creating a small bulge directly underneath the septa, which redirected leaks away from the slit in the bin.

In addition to designing and perfecting the cell, it was necessary to devise a method to insulate the NiTi sample from the grounded, metallic load frame grips in order to perform electrochemical tests. Options that were explored included pairs of scrap rubber; pairs of

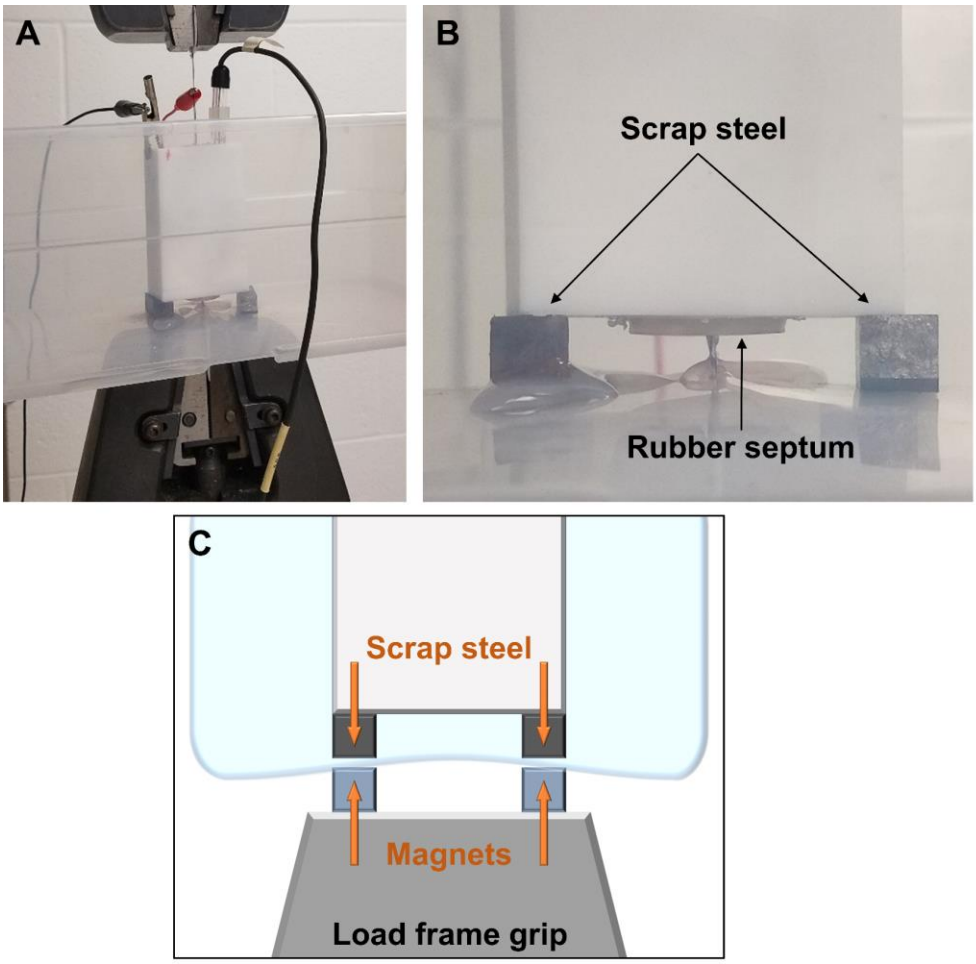

Figure 5: Secondary containment measures. (A) The in-situ cell, three electrode system, and secondary containment mounted in the load frame grips with the sample pulled just taut. (B) A closer view of the bulge in the bin with a demonstration that liquid is prevented from leaking outside of containment, and instead pools. (C) Schematic diagram of method of securing secondary containment to load frame.

sandpaper; leaving the native surface oxide on the tips of the sample rather than polishing them; loose, flat pairs of epoxy (PC-Clear Clear Liquid Epoxy) and fiberglass (Fiberglass Supply Style 7500 x 60" 9.7 oz Plain Weave E-Glass Fabric) composite; and cured epoxy coating. The performance of these grip options (with the exception of scrap rubber and cured epoxy, which failed immediately) were compared (Figure 6A); the sample with the native surface oxide grips served as the control in this comparison. Ultimately, the solution was to lay up both sides of each individual sample between layers of fiberglass and epoxy and allowing them to cure into composite grips (Figure 6B, 6C) (see Chapter III, Procedures). Due to the geometry of the cell,

the sample needed to be laid up on one side, threaded through the slit in the septum, then laid up on the other side (the well would have prohibited achieving an effective vacuum without damaging the vacuum bag). This completed the sample preparation.

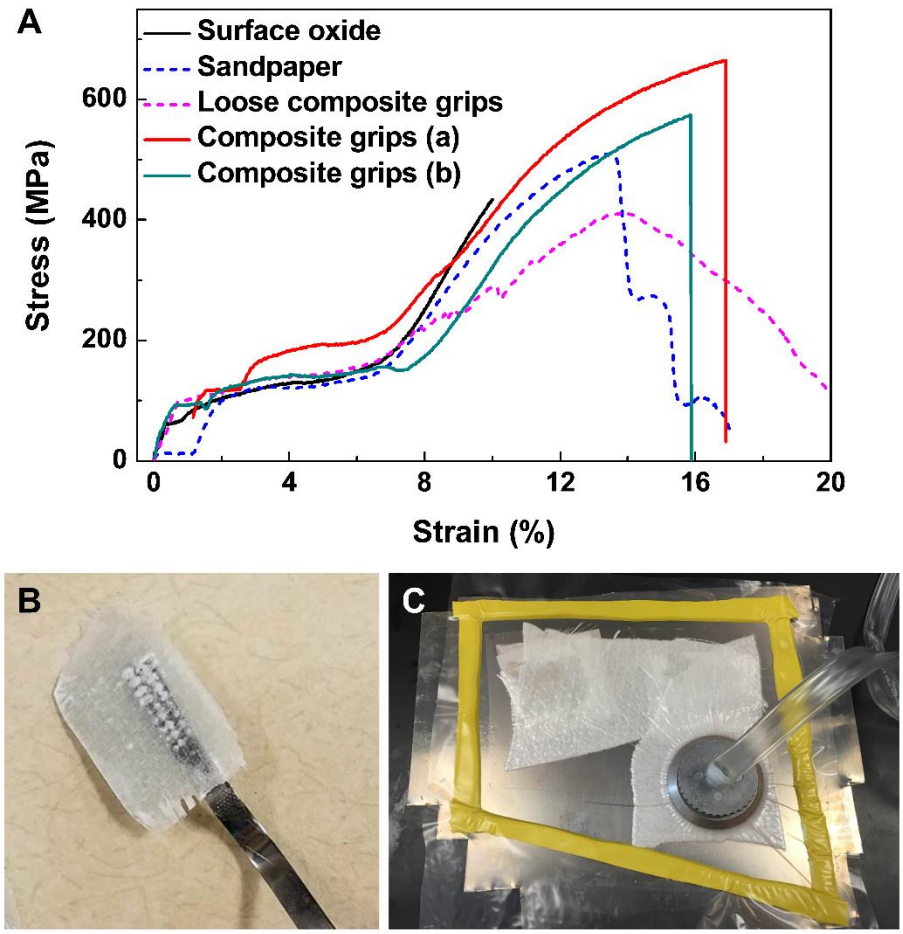

Figure 6: (A) Comparison of stress-strain curves for samples with various types of grips. (B) Photograph of cured composite grip on a sample. (C) Photograph of a completed layup under vacuum.

Heat Transfer and Thermal Effects

After the cell and setup were perfected, it was necessary to confirm that the strain rate employed is quasi-static. Because the sample generates both latent heat during the transformation from austenite to martensite and heat of deformation[2,3,10-13], the strain rate must be slow enough such that the heat transfer out of the sample is on the same order as the rate of heat generation to be considered quasi-static. As long as this process is quasi-static, thermal effects on the electrochemistry can be neglected.

First, the Biot number of the sample was calculated in order to determine if the lumped capacitance transient model is valid ($Bi \ll 0.1$). Because the sample is exposed to both air and aqueous electrolyte, the Biot numbers for both cases (submerged only in air and only in water) were found, and the larger of the two was considered. Thermal properties of NiTi were taken from literature.[3] The calculations are as follows:

$$Bi = \frac{L_C h}{k_B} \tag{1}$$

$$Bi_{water} = \frac{Vh}{Ak_B} = \frac{(150\ mm\ \times 4.5\ mm \times 0.2\ mm) \times 890\ W/m^2 \cdot K}{(2 \times 150\ mm \times 4.5\ mm) \times 20\ W/m^2 \cdot K} = 4.45 \times 10^{-3}$$

$$Bi_{air} = \frac{Vh}{Ak_B} = \frac{(150\ mm\ \times 4.5\ mm \times 0.2\ mm) \times 6.5\ W/m^2 \cdot K}{(2 \times 150\ mm \times 4.5\ mm) \times 20\ W/m^2 \cdot K} = 3.25 \times 10^{-5}$$

where L_c is the characteristic length, h is the convective heat transfer coefficient, and k_B is the thermal conductivity. In both cases, $Bi \ll 0.1$, meaning the lumped capacitance method is valid. Next, the maximum change in temperature was determined for each case (air and water).

The latent heat of transformation is taken from literature[3,12], as is the formula for temperature increase due to heat of deformation[12]. Because the heat transfer coefficient depends in part on the temperature difference between the sample and the reservoir, these calculations were performed iteratively until the temperature used in the heat transfer coefficient matched the

temperature found. This process was not considered for the Biot number calculation because the order of magnitude of the Biot number would not have been significantly affected by these small refinements in the heat transfer coefficient. The change in temperature from heat of deformation is calculated as follows:

$$\Delta T_d = \oint \frac{\beta}{\rho \bar{C}} \sigma d\varepsilon \tag{2}$$

$$\Delta T_d(9.2\%) = \frac{1}{6450\, kg/m^3 \times 500\, J/kg \cdot K}(40.36\, MPa) = 12.51\, K$$

where β is the fraction of deformation work converted to heat (assumed to be 1[12]), ρ is the density, C is the heat capacity, and the integration of σ dε is that of the stress-strain curve. The integration was performed on the data set for a sample strained to 9.2%. However, this calculation does not account for the extended time taken to perform this deformation and the considerable heat transfer to surroundings. The energy released due to deformation over the course of straining is related to the temperature change by the mass (m) and specific heat (c_p) of the specimen.

$$E_d = c_p m \Delta T \tag{3}$$

$$E_d = 500\, J/kg \cdot K \times 12.51\, K \times 8.71 \times 10^{-4}\, kg = 5.45\, J$$

The latent energy released from the transformation is calculated as follows:

$$E_l = LV \tag{4}$$

$$E_l = 4.3 \times 10^7\, J/m^3 \times 1.35 \times 10^{-7} m^3 = 5.81\, J$$

These energy values are added together and divided by the duration of the test to determine the average energy generation rate ($\dot{E}_g$) for use in the transient lumped capacitance calculation. The lumped capacitance method is as follows:

$$\frac{T - T_\infty}{T_i - T_\infty} = e^{-at} + \frac{b}{a(T_i - T_\infty)}(1 - e^{-at}) \tag{5}$$

where $a = \frac{hA_s}{\rho Vc}$ and $b = \frac{q"A_s + \dot{E_g}}{\rho Vc}$. In these expressions, V is the volume of the specimen, A_s is the surface area, and q" is the heat flux from the sample. The initial temperature of the sample is taken to be equal to that of the reservoir (room temperature). This quantity is multiplied through, reducing the equation to:

$$\Delta T = \frac{b}{a}(1 - e^{-at}) \quad (6)$$

After iterative calculations, the maximum temperature change for a sample strained at $1 \cdot 10^{-4}$ s^{-1} ($\dot{E}_g = 2.25 \times 10^{-2}\ W$) in air was found to be ~2.06 K, while that in water is ~0.096. That for a sample strained at $5 \cdot 10^{-4}$ s^{-1} ($\dot{E}_g = 1.13 \times 10^{-1}\ W$) in air is ~7.54 K, and in water is ~0.35 K. It can therefore be assumed that the actual increase in temperature falls somewhere between these values for each case.

Once this maximum change in temperature was determined, a heated experiment was conducted to determine the relationship between change in temperature and change in OCV. A polished, unstrained sample of NiTi, a Platinum counter electrode, a reference electrode (SCE), and a thermocouple were placed in 1 M KOH on a hot plate. The OCV (Figure 7) was monitored at room temperature (21.9°C) as measured by the thermocouple until it stabilized, at which time (~110 seconds) the hot plate was set to 25°C. The OCV was again allowed to stabilize. The stable temperature measurement from the thermocouple was 25.1°C after 900 seconds. The oscillations seen in this graph are from electrical noise in the system from the surrounding building and especially from being placed directly on a hot plate, and the large anomalies correspond to the removal of the thermocouple.

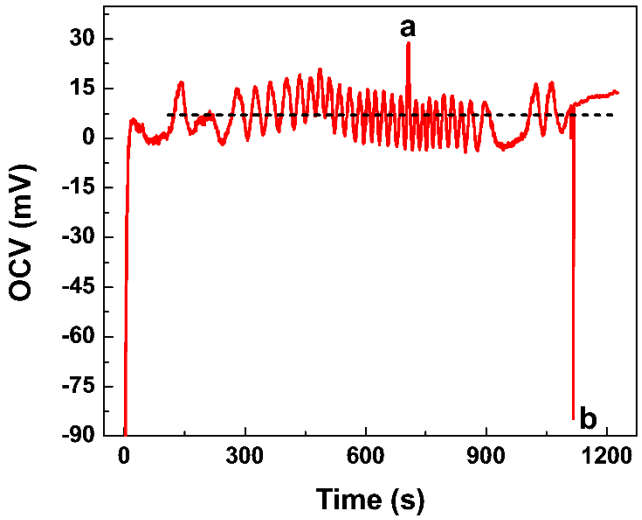

Figure 7: OCV versus time graph for a sample slowly heated to 25.1°C from room temperature. Point "a" corresponds to a point at which the thermocouple briefly broke contact with the electrolyte. Point "b" corresponds to when the thermocouple was removed. Other fluctuations are attributed to small movements of the thermocouple. The dotted line shows the average value after heating began (about 150 seconds).

Accounting for outliers related to the thermocouple, the average increase in OCV over fifteen minutes of heating by 3.2 K was 7.09 mV. A linear extrapolation of this experiment indicates that a 2.06 K temperature increase corresponds to a 4.56 mV increase in OCV, and a 0.1 K temperature increase corresponds to a 0.22 mV increase in OCV (the dynamic rate would result in an increase of 0.78-16.71 mV assuming a linear relationship). Again, it can be assumed that the actual change lies somewhere between these values, both of which are insignificant in comparison to the changes in OCV observed during straining (see Chapter III, Results). Therefore, the thermal effects for quasi-static strain rates are considered to be negligible.

CHAPTER III

EXPERIMENTATION

Procedures

Samples of as-drawn, superelastic Nitinol strips (oxide, thickness ~4.5 mm, width ~0.2 mm) of approximately 50.6-51.0 atomic percent Nickel obtained from Confluent Medical Technologies were cut into ~150 mm lengths. These samples were activated by aging them in atmosphere at 600°C for two hours using a Thermolyne Furnace F30400, then quenching them in water. The surface oxide was then polished off using a rotary polishing wheel with Buehler Whitefelt and 5μm Aluminum Oxide slurry, then with Buehler MicroCloth and 1 μm Alpha Aluminum slurry. The samples were sonicated in ethanol and water for five minutes each.

One side of the NiTi samples were laid up into epoxy and fiberglass in batches. Four rectangular pieces of fiberglass ~5 cm x 10 cm were cut per sample. The epoxy was mixed and spread onto two pieces of fiberglass per sample. These pieces were layered on top of peel ply (Fiberglass Supply Econo-Ply J, 1.6 oz x 60”), then the end of the NiTi sample was placed on top of them. Two more layers of fiberglass and epoxy were placed on top of the sample aligned with the bottom layers. The entire layup was then covered with another layer of peel ply, as well as a layer of cotton breather (Fiberglass Supply Airweave N4 Breather). The layup was sealed beneath vacuum bagging material (Fiberglass Supply Stretchlong 800 x 60” Roll, 200) using vacuum tape, and was then placed under vacuum and allowed to cure for several hours (Figure 6C). Once the batch of free samples was cured, one sample was fitted with a septum with a slit cut through and a small piece of vacuum tape, then pushed through the septum attached to the cell and the cell itself until the vacuum tape flattened into a uniform disc between the two septa. The bare end of the sample was then laid up into composite grips (Figure 6B) using the same process.

The cell, now attached to the sample, was loaded into the grips of an Instron TTC-02ML load frame and the separation was adjusted until the strip was just taut. The cell was filled with 35 mL of 1 M KOH. The electrochemical tests were performed with a Metrohm Autolab PGStat101 using the Monitor OCV procedure. The OCV was monitored using Platinum foil as a counter and a Saturated Calomel Electrode (SCE) as a reference. The mechano-electrochemical experimentation can be visualized as in Figure 8. The Initial State encompasses the time from which the monitoring begins until the OCV stabilizes. Once the system reached a steady state OCV, straining using a flat tensile test method commenced (In-Situ Measurement). The constant extension rate [mm/s] of this test was calculated for each sample individually based on the length of the sample such that the strain rate was $1 \cdot 10^{-4}$ s^{-1} for quasi-static trials or $5 \cdot 10^{-4}$ s^{-1} for increased rate trials. Samples were strained to a predetermined point within each Stage of the Nitinol strain profile: elastic deformation; during the SIM plateau; or until mechanical yield (sudden drop in load without physical separation or other damage of the sample). All strain percentages are in terms of engineering strain. Upon reaching the designated point, the tensile test procedure was terminated and the system was again allowed to reach a steady state OCV (Final State). All experimentation was performed at room temperature.

Three NiTi samples – one polished and unstrained; one polished, unstrained, and soaked in 1 M KOH for one hour, and one polished and strained in 1 M KOH in a three electrode system – were characterized using Raman (Reinshaw) spectroscopy with a 532 nm laser at 5% power for 1800 s exposures. Four NiTi samples – one polished, unstrained, and soaked in 1 M KOH for one hour; one each strained to Stages I, II, and III in 1 M KOH in a three electrode system – were characterized using XRD (Scintag XGEN 4000) with using a wavelength Cu Kα = 1.542 A° and step size of 0.1° between 10° and 60°.

Results

Superelastic NiTi follows a characteristic stress-strain profile (Figure 1) defined by three Stages, which are caused by the SIM phase transformation. The parent phase of NiTi is austenite, a cubic structure which initially deforms elastically. After a critical amount of strain is imparted, the sample reorients via a phase transformation to monoclinic martensite. During this transformation, the load reaches a plateau and austenitic and martensitic phases coexist. Once the martensitic transformation is complete, the sample undergoes de-twinning, then deforms plastically (bonds break and planes slip, meaning this deformation is not recoverable). These Stages are the basis for the choice in strain percentages at which to terminate the sample extension; that is, several samples were deformed to within Stage I, some to within Stage II, and some to within Stage III for assessment of steady state electrochemical behavior.

The OCV of a material is a property of electrical equilibrium and a measure of passivation, as it is the voltage at which the rates of anodic and cathodic reactions are equivalent.[4,22] It is a quantity used in corrosion analysis.[4,28] The OCV was measured before, in conjunction with, and after straining; these states and the corresponding OCV response are illustrated in Figures 8A and 8B, respectively. The OCV data is adjusted such that t=0 corresponds to the moment steady

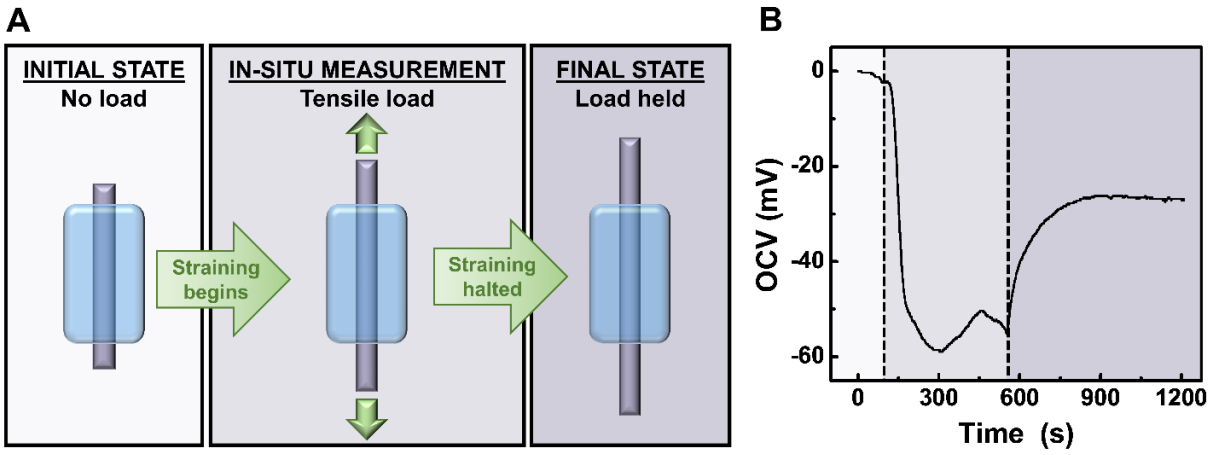

Figure 8: Schematic depiction of testing procedure and corresponding OCV behavior. (A) Diagram of the three States of experimentation. (B) OCV versus time graph color-coded to indicate State.

state was reached, approximately 50 seconds before straining began, by a simple subtraction performed on all values. It is also adjusted such that the initial steady state value (measured vs. SCE) is set to zero; this was also achieved by performing subtraction on all values. Thus, all y-values on this graph represent change in OCV from steady state/no load value, and OCV curves from multiple samples can be more easily compared. A representative full OCV profile can be found in the Appendix.

Figures 9A-9D show the OCV response (adjusted in the same way as that in Figure 8B) overlaid with the load profile for several samples strained to different final strains. The data is aligned accurately on the x-axis by adding the amount of time the OCV test had been running

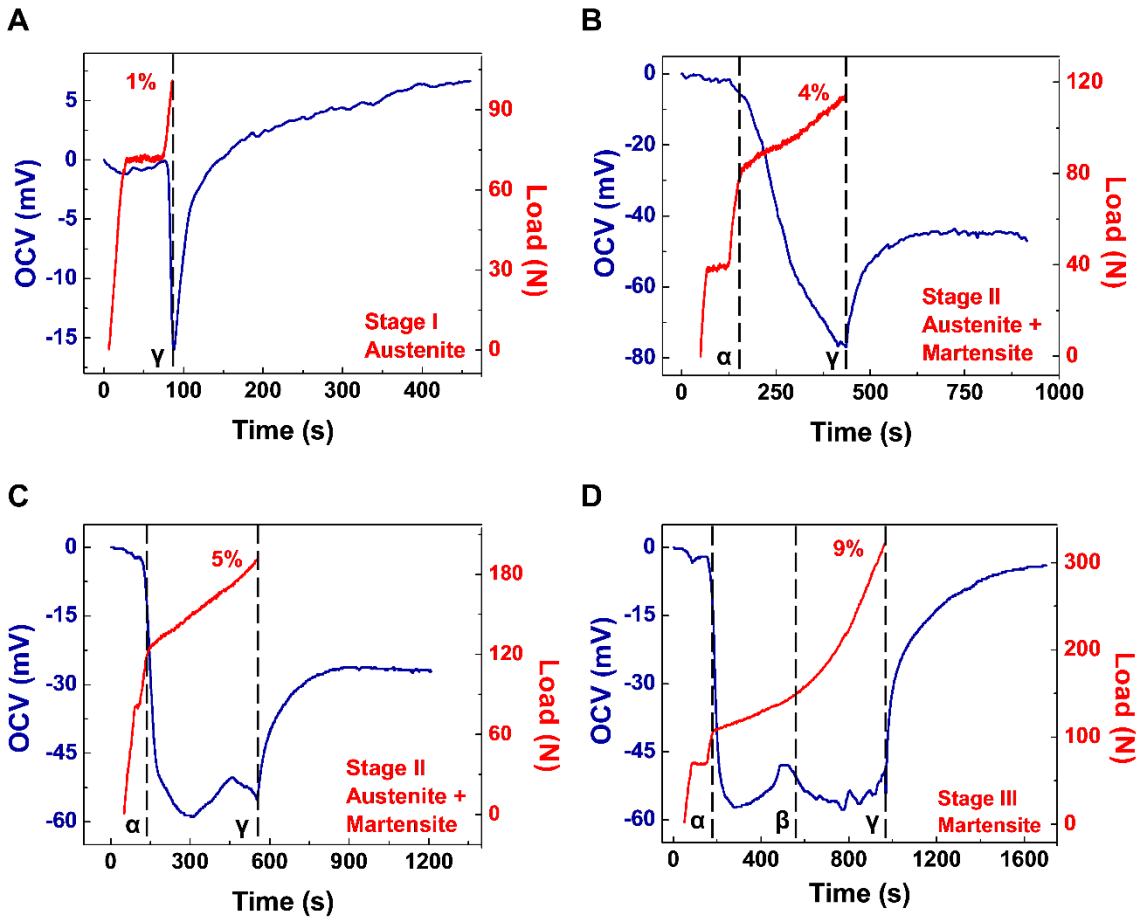

Figure 9: Adjusted OCV and tensile load plotted against time during the In-Situ Measurement State and Final State of experimentation for samples strained to (A) 1% (Stage I), (B) 4% (Stage II), (C) 5% (Stage II), and (D) 9% (Stage III).

when straining began to every time value in the strain data. All samples in this figure were strained at a quasi-static rate of $1 \cdot 10^{-4}$ s^{-1}. The dashed lines represent milestones in the strain profile and delineate the immediacy of the OCV response.

A summary of all possible paths of the straining process and the commensurate behavior of the OCV within each Stage of the strain profile is shown in Figure 10. Each dashed line in Figures 9A-9D is labelled with a corresponding step found in Figure 10. During Stage I, the OCV

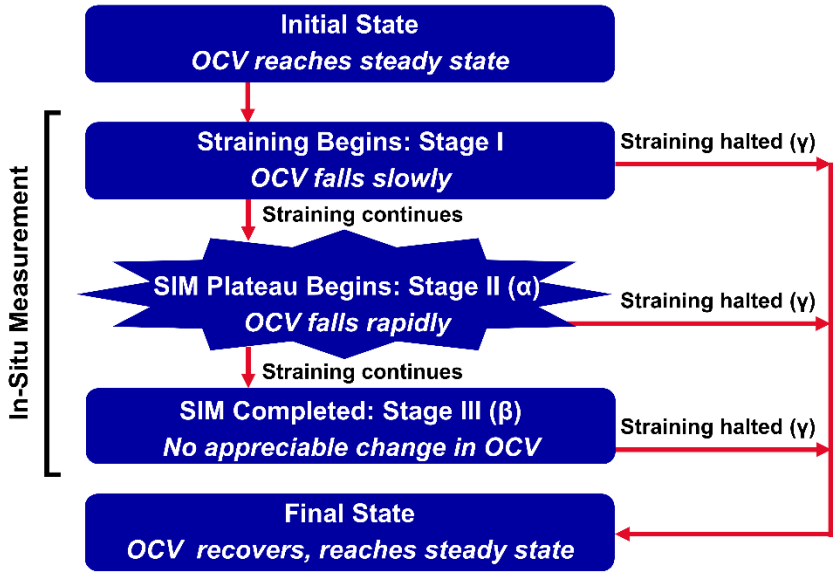

Figure 10: Summary of all possible paths of experimentation with OCV response during each State of experimentation as well as each Stage of deformation.

begins to fall a small amount, fewer than ~10 mV. Once the sample enters Stage II, the SIM plateau, the OCV instantly plummets ~50 mV in response to the formation of the shear band front[4,22] before the rate of decrease slows slightly, falling another ~10 mV. During this plateau, the OCV eventually reaches a minimum value (maximum change from steady state), after which the OCV also plateaus while possibly experiencing local minima and maxima. This flat response is in agreement with the findings of Racek et al.[22] It is suspected that these miniature peaks and valleys correspond to the discontinuous and highly localized nature of the small portion of martensitic transformation that occurs outside of the shear band front in remaining pockets of austenite.[1-4,9,26]

After the conclusion of the SIM transformation (entry into Stage III), the OCV does not significantly recover. Extension of the sample was ceased (without removing load) at different strain percentages. Regardless of the Stage at which straining ceased, the OCV instantaneously and rapidly began to recover. In some cases, the new steady state value was approximately equivalent to that of the Initial State before straining (zero net change in OCV); in others, the new value fell significantly above or below that of the Initial State (non-zero net change in OCV).

In order to examine the steady state behavior of a sample with load removed, a trial was performed in which the sample was strained at a quasi-static rate to 4% (comparable to that in Figure 9B) then severed instantaneously (Figure 11). It can be seen that during the brief delay between terminating the strain procedure (α) and cutting the sample (spike in OCV curve), the OCV began to recover slightly. Severing the sample allowed it to recover an unknown amount of its extension, and resulted in a negligible change in steady state OCV. This, taken with the results shown in Figures 9B and 9C, seems to indicate that maintaining extension is amongst the prerequisites for permanently altering the OCV.

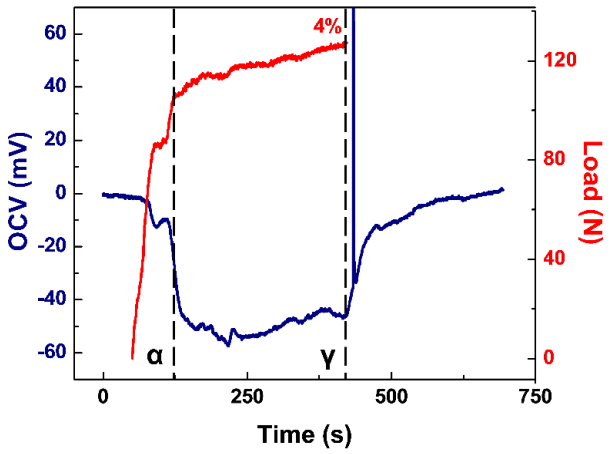

Figure 11: Plot of OCV and tensile load versus time for a sample that was severed after reaching the desired strain to demonstrate steady-state behavior of a sample with load removed. The spike in OCV corresponds to when the sample was severed instantaneously. Point α is where the strain procedure was terminated. The spike in OCV corresponds to when the sample was severed.

The XRD and Raman spectroscopy characterizations of the samples are shown in Figures 12A and 12B, respectively. Samples were examined in XRD to characterize the bulk of the specimen. These samples include an unstrained sample that was soaked in 1 M KOH for one hour

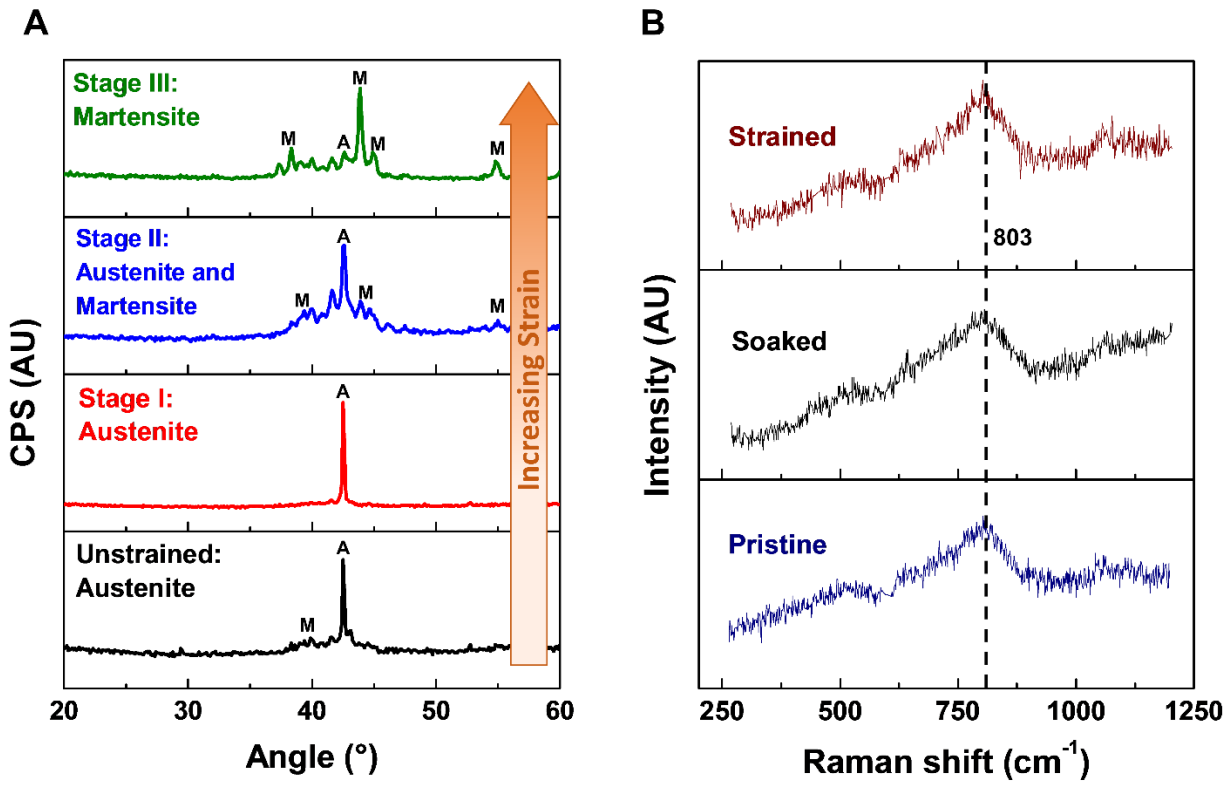

Figure 12: Characterization of samples. (A) XRD spectra of unstrained NiTi soaked in 1 M KOH for one hour and samples of NiTi strained to Stages I, II, and III in the three electrode system. The austenitic peaks are denoted "A," while the martensitic peaks are denoted "M." (B) Raman spectra taken with a 532 nm laser at 5% power for 1800 s exposures of pristine (polished, unstrained, never exposed to KOH) NiTi, unstrained NiTi soaked in 1 M KOH for one hour, and NiTi strained in the three electrode system.

and samples strained to Stages I, II, and III in the three electrode system. All of the samples exhibit an austenitic peak at 43° corresponding to the (100) plane (JCPDS no. 18-0899), although this peak is weak in the Stage III sample. The martensitic peaks exhibited by the Stage II and Stage III samples include 44°, 45°, and 55°, which correspond to the (020), (111), and (120) planes, respectively (JCPDS no. 35-1281). Additional peaks appear in the Stage II sample at 39° from the (002) plane and in the Stage III sample at 38° from the (110) plane (JCPDS no. 35-1281. The presence of martensitic peaks in the unstrained sample may be a product of polishing and cutting

the sample. It appears that martensite reverts to austenite after the miniature plateau seen in Stage I (Figure 1), which is supported by the sharp austenitic peak and complete absence of martensitic peaks for the Stage I sample, which was strained to past this miniature plateau. Samples were examined with Raman spectroscopy in order to characterize the surface of the specimens. These samples include a pristine and unstrained sample that was not soaked in KOH, an unstrained sample that was soaked in 1 M KOH for one hour, and a sample that was strained in the three electrode system. The main peak of each of these spectra occurs at 803 cm^{-1} corresponding to a native surface oxide, and the shapes of the spectra do not show significant differences. This suggests that the electrochemical response to straining does not occur due to the formation, dissolution, or other change in composition of a chemical species.

A rate study was also performed using this in-situ mechano-electrochemical test method. The stress-strain curves obtained from straining two samples to Stage II (Figure 13A) and Stage The corresponding OCV curves are shown in Figures 13C and 13D. These graphs are adjusted like those in Figures 8B and 9A-9D; additionally, the time scale for the samples strained at $1 \cdot 10^{-4}$ s^{-1} was multiplied by a ratio of the extension rate of the higher strain rate sample to the extension rate of the sample in question, such that the two data sets would be visually comparable. It is evident in both Figures 13C and 13D that the maximum change in OCV is 2.5-2.9x larger for samples strained at a 5x higher rate. It can also be seen that, even when corrected for time scale, the samples strained at a higher rate take significantly longer in comparison to the duration of the in-situ measurement (1.5-3.8x) to reach steady state. The anomalous local minimum seen in Figure 13D for the higher strain rate corresponds to the deviation from a typical strain profile found between 5-7% seen in Figure 13B. Finally, while the quasi-static trials that were stopped within the SIM plateau experienced a permanent negative change in steady state OCV of varying magnitude

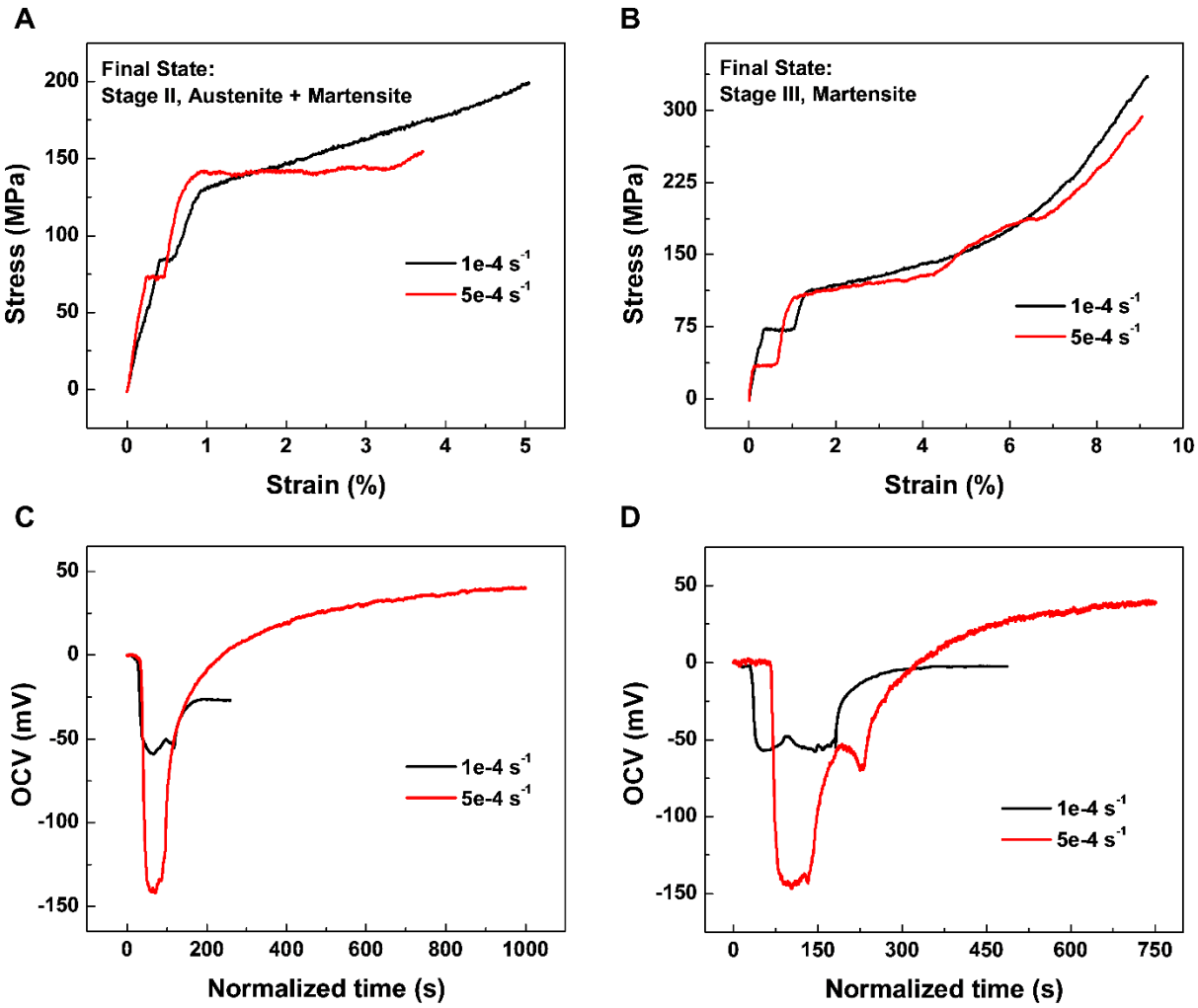

Figure 13: Rate comparison of stress-strain curves at a quasi-static strain rate (1·10-4 s^{-1}) and an increased strain rate (5·10-4 s^{-1}) strained to (A) Stage II and (B) Stage III. The corresponding OCV responses plotted against a normalized time scale for rate comparison of samples strained to (C) Stage II and (D) Stage III.

(Figures 9B and 9C), both dynamic trials experienced a positive change in steady state OCV of about 40 mV. This is likely a product of the increased rate of straining, particularly the likely significant change in temperature (see Chapter II, Heat Transfer and Thermal Effects).

To compare the OCV curves for each trial, they are plotted on the same scale in Figure 14A with the strain profiles that correspond to them shown in Figure 14B for reference. From this plot it can be seen that most samples exhibit identical OCV behavior in Stage I and in entering Stage II, and there is some slight variance in the duration of the miniature stress plateau that occurs

in Stage I. The minimum OCV of all samples with high strain percentages (≥4%) are similar, which agrees with the findings of Racek et al.[4] The length of the Stage II SIM plateau is expected to vary from sample to sample depending on polycrystalline texture, amount of austenite, and degree of de-twinning in martensite.[1,11] Figure 14C shows the change in steady state OCV is plotted versus

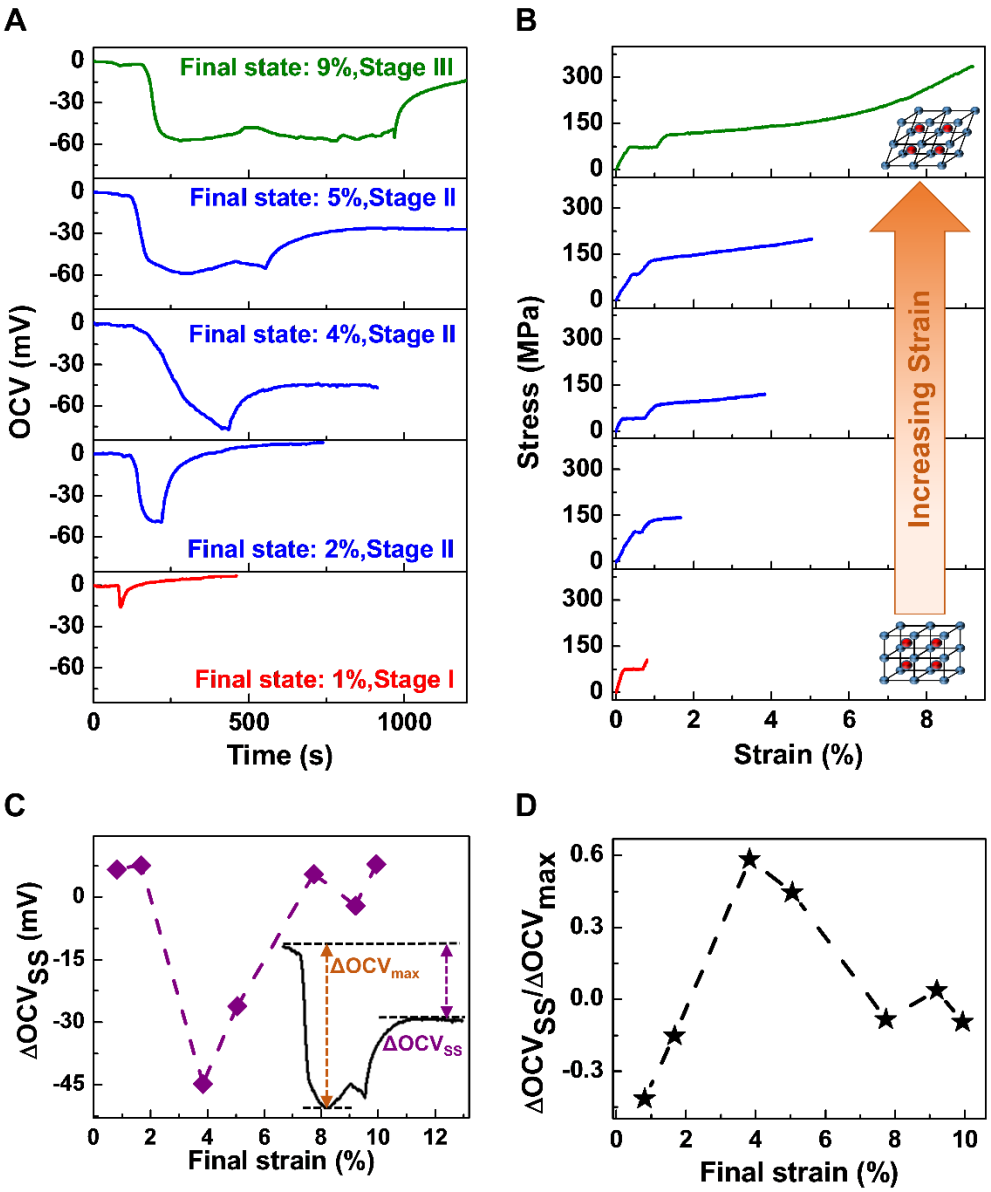

Figure 14: Synthesis of data. (A) OCV responses of samples strained to 1% (Stage I), 2% (Stage II), 4% (Stage II), 5% (Stage II), and 9% (Stage III) at 1·10-4 s-1 plotted on the same scale and (B) the corresponding stress-strain curves for each sample. (C) The change in steady state OCV plotted against the strain percentage to which the sample was deformed. Inset: pictorial representation of the quantities plotted in Figures 14C and 14D on a representative OCV curve. (D) The ratio of the change in steady state OCV to the maximum change in OCV plotted against the strain percentage to which the sample was deformed.

the strain reached and held in the Final State. This quantity is a measure of the permanent alteration of electrochemical properties of the sample while load is held. Figure 14D shows the ratio of the change in steady state OCV to the maximum change in OCV (occurring at the minimum OCV during Stage II), versus the strain reached and held in the Final State. The trend seen in Figure 14C shows a dramatic dip for final strain values that fall within the SIM region (~2-6%). These points represent a much larger magnitude of change in the negative direction than other trials experienced in the positive direction. The trend in Figure 14D shows that final strains outside the SIM plateau correspond to negligible changes in the steady state OCV compared to OCV changes during the transformation, while final strains within the SIM plateau correspond to considerable permanent changes in steady state OCV. It bears noting that samples strained to Stage I or very early in Stage II did not have an opportunity to reach a "true" minimum OCV before strain cessation, meaning the magnitude of the ratio of the steady state OCV change to the max OCV change should be smaller.

These trends, taken with information from the Raman characterization and heat transfer calculations, indicate that the mechanism of reorientation from austenite to martensite bears an intrinsic energetic signature that has a stark effect on the OCV. Although sample characterization and visual inspection did not suggest the formation of an oxide, it is likely that the NiTi grew a passivating surface while in contact with the air (between polishing and experimentation). Because there is little difference in steady state OCV behavior of trials stopped in Stage I (austenite) and trials stopped in Stage III (martensite), and recalling the Nernst equation ($V = -\frac{\Delta G}{nF}$), it would appear that these two states lie at energetic minima, and are separated by an activation barrier of sorts related to elongation, which can be visualized as in Figure 15A. The absolute value of the ratio of the steady state OCV change to the maximum OCV change is plotted in Figure 15B. The

quantities referenced here are shown illustratively in the inset of Figure 14C. The red marker is an estimate of the value for the 1% trial had it theoretically reached its "true" minimum OCV.

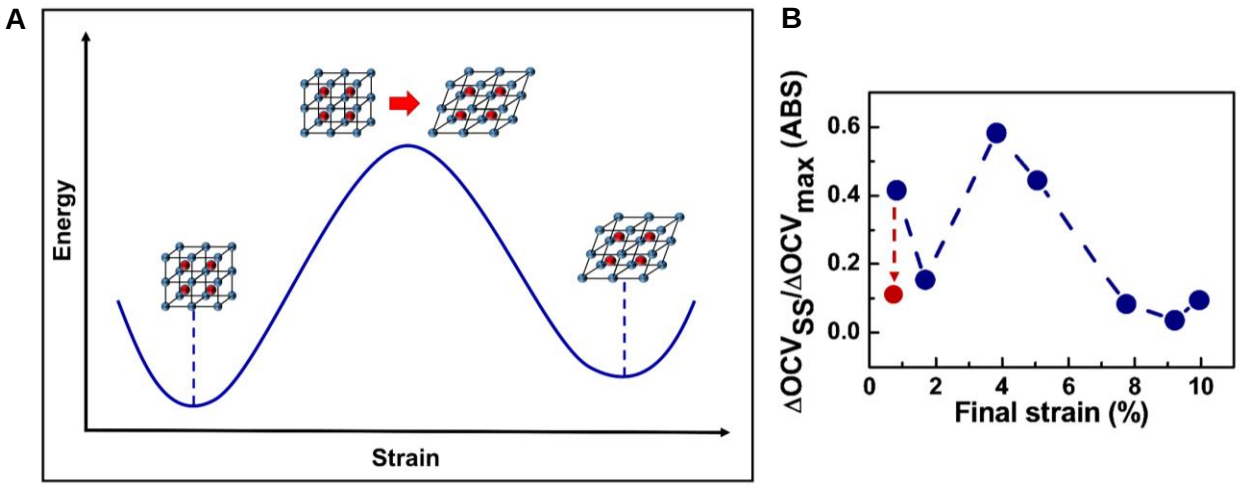

Figure 15: (A) Qualitative depiction of apparent relationship between strain and energetic response. (B) Absolute value of ratio of steady state OCV change to maximum OCV change.

Overall, these experiments demonstrate that the stress-induced phase transformation bears an energetic signature that affects the open circuit voltage of the sample, and can be manipulated such that this effect is permanent. This permanent change is an average of 7.1 mV for samples strained to Stage I, -35.5 mV for those strained to Stage II, and 3.2 mV for those strained to Stage III. Increasing the strain rate fivefold results in an increase in the maximum OCV change by a factor of about 2.5-2.9.

Conclusions

This investigation has yielded a working in-situ electrochemical cell designed to complement a vertical load frame performing flat tensile tests. It has also yielded an insight into the interconnection of mechanics and electrochemistry in the form of the ability to permanently alter electrochemical properties through mechanical strain. This proof of concept shows that the OCV of a superelastic alloy can be reduced predictably based on the extent and rate of tensile deformation and impartation of strain. Such tuning can be accomplished with relatively little energy input – only that necessary to operate a load frame. The ability to raise or lower the open circuit potential of a material without significant energy input has applications in material processing, corrosion, and energy storage. It has also been found that the phase transformation from austenite to martensite is accompanied by an energetic behavior that cannot be explained by thermal effects or by oxide formation, is certainly linked to rate effects. This relationship can be advantageous for reducing the energetic cost of corrosive metal processing.

APPENDIX

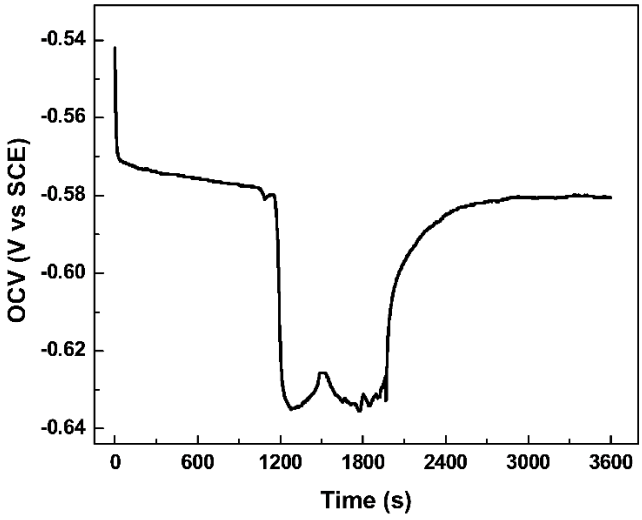

Figure A1: A representative, raw OCV versus time graph (not truncated or adjusted).

REFERENCES

1. G. Tan, Y. Liu, P. Sittner, M. Saunders, Lüders-like deformation associated with stress-induced martensitic transformation in NiTi, Scr. Mater. 50 (2004) 193-198.

2. J. A. Shaw, S. Kyriakides, Thermomechanical aspects of NiTi, J. Mech. Phys. Solids 43 (1995) 1243-1281.

3. P. H. Leo, T. W. Shield, O. P. Bruno, Transient heat transfer effects on the pseudoelastic behavior of shape-memory wires, Acta metal. Mater. 41 (1993) 2477-2485.

4. J. Racek, M. Stora, P. Sittner, L. Heller, J. Kopecek, M. Petrenec, Monitoring tensile fatigue of superelastic NiTi wire in liquids by electrochemical potential, Shap. Mem. Superelasticity 1 (2015) 204-230.

5. S. Miyazaki, K. Otsuka, Y. Suzuki, Transformation pseudoelasticity and deformation behavior in a Ti-50.6at%Ni alloy, Scripta Metall. 15 (1981) 287-292.

6. J. A. Shaw, S. Kyriakides, Initiation and propagation of localized deformation in elasto-plastic strips under uniaxial tension, Int. J. Plast. 13 (1997) 837-871.

7. J. A. Shaw, S. .Kyriakides, On the nucleation and propagation of phase transformation fronts in a NiTi alloy, Acta Mater. 45 (1997) 683-700.

8. Y. Liu, Y. Liu, J. Humbeeck, Lüders-like deformation associated with martensite reorientation in NiTi, Scripta Mater. 39 (1998) 1047-1055.

9. Y. Liu, Y. Liu, J. Humbeeck, Two-way shape memory effect developed by martensite deformation in NiTi, Acta Mater. 47 (1998) 199-209

10. C. Grabe, O. T. Bruhns, On the viscous and strain rate dependent behavior of polycrystalline NiTi, Int. J. Solids Struct. 45 (2008) 1876-1895.

11. D. Entemeyer, E. Patoor, A. Eberhardt, M. Berveiller, Strain rate sensitivity in superelasticity, Int. J. Elasticity 16 (2000) 1269-1288.

12. S. N. Nasser, J. Y. Choi, W. G. Guo, J. B. Isaacs, High strain-rate, small strain response of a NiTi shape memory alloy, J. Eng. Mater. Tech. 127 (2005) 83-89.

13. P. G. McCormick, Y. Liu, Intrinsic thermal-mechanical behaviour associated with the stress-induced martensitic transformation in NiTi, Mater. Sci. Eng. A 167 (1993) 51-56.

14. C. Feng, J. Zhao, F. Yang, K. Gong, S. Hao, Y. Cao, C. Hu, J. Zhang, Z. Wang, L. Chen, S. Li, L. Sun, L. Cui, G. Yu, Nonvolatile modulation of electronic structure and correlative magnetism of L10-FePt films using significant strain induced by shape memory substrates, Sci. Rep. 6 (2016) 20199-20207.

15. K. Yan, T. A. Maark, A. Khorshidi, V. A. Sethuraman, A. A. Peterson, P. R. Guduru, The influence of elastic strain on catalytic activity in the hydrogen evolution reaction, Angew. Chem. Int. Ed. 128 (2016) 6283-6289.

16. M. Du, L. Cui, Y. Cao, A. J. Bard, Mechanoelectrochemical catalysis of the effect of elastic strain on a platinum nanofilm for the ORR exerted by a shape memory alloy substrate, J. Am. Chem. Soc. 137 (2015) 7397-7403.

17. Y. Zhang, C. Luo, W. Li, C. Pan, Strain induced chemical potential difference between monolayer graphene sheets, Nanoscale 5 (2013) 2616-2619.

18. N. Muralidharan, R. Carter, L. Oakes, A. P. Cohn, C. L. Pint, Strain engineering to modify the electrochemistry of energy storage electrodes, Sci. Rep. 6 (2016) 27542.

19. Y. Guo, J. Hu, Y. Jiang, J. Li, Characterization of strain-induced martensite and anodic polarization properties of a newly developed lean duplex stainless steel 2002 after tensile deformation, Int. J. Electrochem. Sci. 11 (2016) 4812-4827.

20. Z. Y. Liu, X. G. Li, Y.F. Cheng, Effect of strain rate on cathodic reaction during stress corrosion cracking of X70 pipeline steel in a near-neutral pH solution, J. Mater. Eng. Perform. 20 (2011) 1242-1246.

21. J. Racek, P. Sittner, L. Heller, J. Pilch, P. Sedlak, L. Kaderavek, Electrochemistry of NiTi wires/springs subjected to static/cyclic loadings, Mater. Today Proceedings 2S (2015) S965-S969.

22. G. Rondelli, B. Vicentini, Evaluation by electrochemical tests of the passive film stability of equiatomic Ni-Ti alloy also in presence of stress-induced martensite, J. Biomed. Mater. Res. 51 (2000) 47-54.

23. C. Montero-Ocampo, H. Lopez, A. Salinas Rodriguez, Effect of compressive straining on corrosion resistance of a shape memory (Ni-Ti alloy in ringer's solution), J. Biomed. Mater. Res. 32 (1996) 583-591.

24. H. H. Huang, Corrosion resistance of stressed NiTi and stainless steel orthodontic wires in acid artificial saliva, J. Biomed. Mater. Res. 66 (2003) 829-839.

25. C. Heßing, J. Frenzel, M. Pohl, S. Shabalovskaya, Effect of martensitic transformation on the performance of coated NiTi surfaces, Mater. Sci. Eng. A 486 (2008) 461-469.

26. L. Neelakantan, B. Schönberger, G. Eggeler, A. W. Hassel, An in situ tensile tester for studying electrochemical repassivation behavior: Fabrication and challenges, Rev. Sci. Instrum. 81 (2010) 033902.

27. C. H. Huang, J. C. Huang, J. B Li, J. S. C. Jang, Simulated body fluid electrochemical response of Zr-based metallic glasses with different degrees of crystallization, Mater. Sci. Eng. C 33 (2013) 4183-4187.